Journal of Nuclear Materials 406 (2010) 244–250

Contents lists available at ScienceDirect

Journal of Nuclear Materials

journal homepage: www.elsevier.com/locate/jnucmat

Atomic scale investigation of radiation-induced segregation in austenitic stainless steels

A. Etienne [a,b,*], B. Radiguet [a], N.J. Cunningham [b], G.R. Odette [b], P. Pareige [a]

[a] Groupe de Physique des Matériaux, Université et INSA de Rouen, UMR CNRS 6634, BP 12, 76 801 Saint Etienne du Rouvray Cedex, France
[b] Materials Department, University of California, Santa Barbara, CA 93106, USA

ARTICLE INFO

Article history:
Received 8 June 2010
Accepted 27 August 2010

ABSTRACT

Radiation-induced precipitation and segregation in a cold-worked 316 austenitic stainless steel irradiated with 10 MeV Fe^{5+} ions were characterized by atom probe tomography. Ni and Si enrichment and Cr depletion were observed in roughly spherical and torus-shaped clusters, believed to be due to solute enrichment and depletion at dislocation loops. Solute segregation was also observed at network dislocations. These observations are consistent with the phenomenon of radiation-induced segregation. Radiation-induced segregation at grain boundaries was also studied at the near atomic scale. Comparison of these observations with results from the literature shows a difference in the magnitude of the peak concentration of segregated solutes.

1. Introduction

Austenitic stainless steels, commonly used in internal structures of light water reactors, are susceptible to irradiation assisted stress corrosion cracking (IASCC). This complex phenomenon is still not well understood and is mediated by many types of variables, such as those that describe: (a) the corrosive chemical environment; (b) the applied stresses; and (c) the material and associated evolution of the alloy microstructure and microchemistry under irradiation [1,2]. IASCC in austenitic stainless steels is most often associated with radiation-induced segregation (RIS) at grain boundaries (GB) [1]. Thus, RIS has been extensively studied for the two last decades [3–10] for both neutron and ion irradiated alloys. Ion irradiations cannot directly simulate neutron conditions, particularly due to large differences in the damage rates and, in some cases, bulk versus near surface behaviour. However ion irradiations have provided critical mechanistic insight on IASSC and RIS and have the distinct advantage of being well controlled, while avoiding the costs and complications of dealing with highly radioactive specimens.

RIS at GB is generally characterized by Energy Dispersive X-ray spectroscopy (EDX) in a Scanning Transmission Electron Microscope (STEM), or Auger Electron Spectroscopy (AES). AES is typically used to measure grain boundary composition but not segregation profiles [11]. However, solute enrichment or depletion on planes near the GB is very important, and provides information of RIS mechanisms. It should also be mentioned that the contribution of adjacent planes to grain boundaries often induces an underestimation of the segregation intensity [4,12]. Concentration profiles are obtained using STEM/EDX. The spatial resolution for EDX, determined by the finite probe width and the beam broadening, is rarely better than 2 nm [12,13]. Such STEM/EDX averaging cannot resolve finer scale details of the GB concentration profiles and, hence, may underestimate the actual peak magnitude of the segregation [4]. Further, the electron beam has to be parallel to a well-aligned "edge-on" GB to avoid overlap with matrix in the probed volume [11,14]. In the better case, Atom Probe Tomography can reach near atomic spatial resolution (<0.5 nm and ~0.2 nm respectively perpendicular to and along analysis direction). Thus a primary objective of this work was to use atom probe tomography to characterize radiation-induced segregation at GBs at the near atomic scale.

It has been shown recently that neutron irradiation induces the formation of Ni–Si enriched clusters in a 316 SS [15]. The authors suggest that the solute clusters are formed by radiation-induced segregation to dislocation loops. Although this conclusion was also supported by TEM and atom probe tomography studies of ion irradiated stainless steels [16], a second objective of this work is further characterize the Ni–Si enriched clusters and evaluate the mechanisms responsible for their formation.

A description of the material and experimental technique is given in Section 2 followed by the results in Section 3 that are then discussed in Section 4.

2. Experimental

The alloy composition of the 15% cold-worked 316 austenitic stainless steel (CW 316 SS) is given in Table 1. A previous atom

* Corresponding author at: Groupe de Physique des Matériaux, Université et INSA de Rouen, UMR CNRS 6634, BP 12, 76 801 Saint Etienne du Rouvray Cedex, France. Tel.: +33 2 32 95 51 40; fax: +33 2 32 95 50 32.
E-mail address: auriane.etienne@univ-rouen.fr (A. Etienne).

0022-3115/$ - see front matter © 2010 Elsevier B.V. All rights reserved.
doi:10.1016/j.jnucmat.2010.08.043

Table 1
Bulk composition of the CW 316 SS. Values are given both in atomic and weight percents. Balance is iron. Values are given by the steelmaker.

	C	P	Si	Cr	Ni	Mo	Mn	Cu	Co
wt.%	0.054	0.027	0.68	16.60	10.60	2.25	1.12	0.24	0.12
at.%	0.25	0.048	1.34	17.70	10.02	1.30	1.13	0.21	0.113

probe tomography study on this alloy in the unirradiated condition showed a homogeneous solute distribution [15].

A plate of 10 × 10 × 0.25 mm thick coupon was sectioned and wet polished with silicon carbide paper. The coupon was electro-etched at 5 V and ≈20 mA for about 5 min in an aqueous solution of 60% HNO_3 to reveal the grain boundaries. The coupon was then irradiated with 10 MeV Fe^{5+} ions in the JANNuS facility of the CEA in Saclay [17,18] at 350 °C. The irradiation conditions are summarized in Table 2. Based on the SRIM 2006 code (http://www.srim.org/) [19] and the Kinchin Pease approximation, the experimental dose and dose rate are estimated to be 10 dpa and 5.6×10^{-4} dpa s^{-1}, respectively. As shown in Fig. 1, the SRIM calculations show that a 10 MeV Fe^{5+} irradiation results in a nearly uniform dpa and dpa rate to a depth of ≈1 μm.

Atom probe needles were micromachined using a FEI Helios 600 dual beam scanning electron microscope/focused ion beam (SEM/FIB) instrument following the procedure described in [20]:

(i) A protective platinum cap of 0.1 μm in thickness is deposited, in this case, over the region containing a grain boundary.
(ii) A Ga ion beam milled section of the region is fabricated by a lift-out procedure. First, a slot about 2.5 μm wide and ≈20 μm length is milled at a coupon tilted ≈−30° with respect to the ion beam direction, to a shallow depth of ≈1 μm. A second slot is then milled after rotating the coupon 180° to form a wedge shaped slice blank. One side of the wedge slice is then cut free and the lift-out wedge is attached with a platinum deposit using a micromanipulator probe. The second side of the lift-out is then cut free, resulting in an equilateral wedge shaped specimen blank.
(iii) Several atom probe needles blanks are then milled out along the length of the wedge. The rough needle blanks are then attached to Si posts, on a holder containing an array of posts, using platinum deposit.
(iv) The rough needle blanks are then annular Ga–ion milled into sharp APT needle tips. Care is taken to be sure that the milled sharp needle is taken from the uniformly damaged depth of 1 μm. The final milling was performed Ga beam energy of 2 keV at a current of about 28 pA.

APT measurements were performed using an Imago Local-Electrode Atom Probe (LEAP) 3000X HR. The LEAP measurements were performed at 77 K, using green (λ = 532 nm) ultra-fast laser pulses with a 200 kHz repetition rate at a voltage bias between 2 and 6 kV. The equivalent pulse fraction was estimated to 20%. The *x*–*y* positions of field-emitted atoms are recorded on a 2D channel plate detector. The isotopic mass to charge ratio for each detected ion was determined by a time of flight measurement. The *z*-position is estimated based on the sequence of atom emissions assuming uniform layer-by-layer evaporation. The corresponding elemental atom positions in the 3D volume were reconstructed

Table 2
Irradiation conditions. Dose in dpa is estimated using SRIM 2006 calculations.

Temperature (°C)	Dose rate (m^{-2} s^{-1})	Dose (m^{-2})	Dose rate (dpa s^{-1})	Dose (dpa)
350	2.6×10^{16}	4.7×10^{20}	5.6×10^{-4}	10

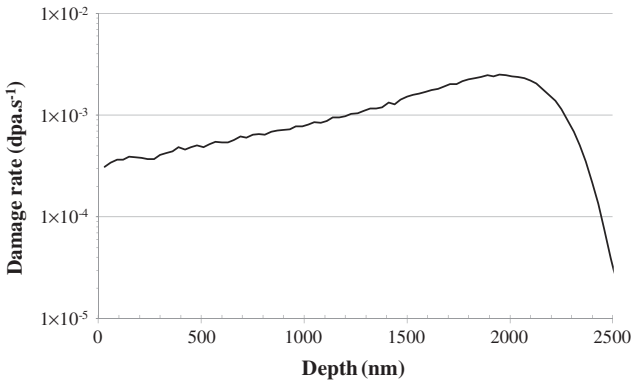

Fig. 1. Irradiation damage rate of 10 MeV Fe^{5+} ions as a function of the depth, calculated with SRIM software.

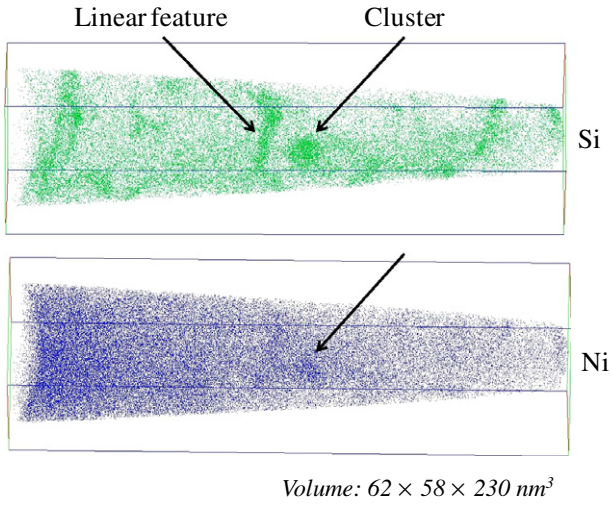

Fig. 2. 3D reconstruction of the APT data obtained in the Fe^{5+} ion irradiated 316 SS showing linear features and 3D clusters enriched with Ni and Si.

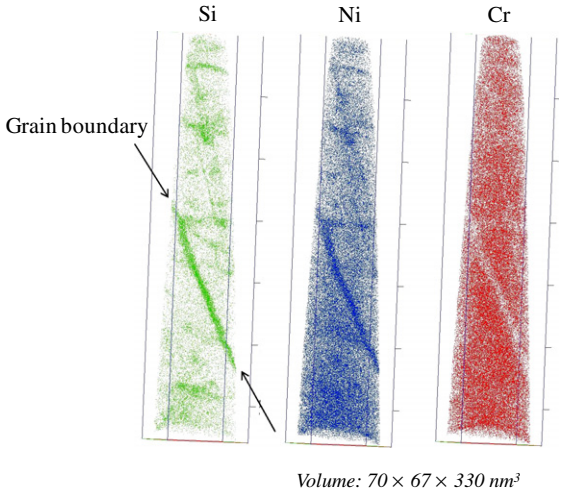

Fig. 3. APT data showing Ni/Si segregation and Cr depletion at a grain boundary in the Fe^{5+} ion irradiated 316 SS.

using the LEAP Imago Interactive Visualization and Analysis Software (IVAS) and complemented by the analysis software developed at the University of Rouen.

3. Results

After ion irradiation, the solute distribution is clearly heterogeneous in the reconstructed volumes (Figs. 2 and 3). First, as shown in Fig. 2, both cylindrical 1D feature and rounded or torus-shaped 3D clusters, enriched in Si and Ni, are present. Si and Ni segregation (enrichment) and Cr depletion at grain boundary region slabs that cut across the needle are also clearly evident, as illustrated in Fig. 3. Note, it is easy to distinguish the cylindrical from the slab features by eye when the 3D distributions are rotated.

The compositions and enrichment factors (the ratio of the concentration in the enriched region relative to the matrix concentration) of the different features are summarized in Table 3. All the features are enriched in Si, Ni and P, while they are depleted in Cr. The matrix composition of the ion irradiated 316 SS is also given in Table 3. The matrix composition is determined from the global mass spectrum, by removing atoms located into 3.1 at.% Si isosurfaces. As expected from mass balance considerations, the matrix is measurably depleted in Ni and Si and slightly enriched in Cr.

3.1. Cylindrical features

The cylindrical features are highly enriched in Si, Ni and P. Peak concentrations of Si and Ni reach 9.8 at.% (from 1.1 at.%) and 26.1 at.% (from 8.5 at.%), respectively, while the Cr concentration decreases to 10.4 at.% (from 18.2 at.%). Considering their shape, the cylindrical features are certainly associated with Ni, Si and P segregation and Cr depletion at network dislocations. The cylindrical diameters of the segregated regions range from ≈4 to 8 nm. The linear density of the cylinders is about 5×10^{14} m^{-2}, which is very consistent with the dislocation density in CW 316 stainless steel.

3.2. Solute clusters

Two kinds of 3D solute clusters are present in reconstructed volumes. As shown in Fig. 4a some clusters have rounded shapes, while Fig. 4b shows that others are torus-shaped. The Ni–Si rounded clusters were previously observed in the neutron irradiated 316 SS [15]. They have a lenticular shape. However, since most of them are intercepted on the edge of the needle, it is difficult to determine an accurate cluster size. The rounded cluster in Fig. 4a is between 10 and 15 nm in length and 6 and 8 nm in thickness. The number density of Ni–Si rounded clusters is $\approx 1.0 \pm 0.6 \times 10^{22}$ m^{-3}. As seen in Fig. 4a, P segregation is, in some cases, visible

Table 3
Composition of the matrix and the different features observed in Fe^{5+} ion irradiated 316 SS samples. The enrichment factor F is given by the ratio of the concentration in the feature over the matrix concentration. Errors are given by the standard deviation 2σ. Balance is iron.

		C	P	Si	Cr	Ni	Mn	Co	Mo	Cu
Matrix composition	at.%	0.29	0.04	1.1	18.2	8.5	0.8	n.s.	1.5	0.2
Segregation on dislocations	at.%	0.12	0.22	9.8	10.4	26.1	0.5	0.7	0.8	n.s.
	2σ	*0.06*	*0.08*	*0.5*	*0.5*	*0.8*	*0.2*	*0.2*	*0.2*	–
	F	0.4	5.5	8.9	0.6	3.1	0.6	n.s.	0.1	n.s.
	ΔF	*0.2*	*2*	*0.5*	*0.1*	*0.1*	*0.3*	-	*0.1*	–
Lenticular rounded Ni–Si clusters	at.%	0.04	0.4	12.3	10.2	28.2	0.5	0.6	0.5	0.2
	2σ	*0.03*	*0.1*	*0.5*	*0.5*	*0.7*	*0.2*	*0.2*	*0.2*	*0.1*
	F	0.1	10	11.2	0.6	3.3	0.6	n.s.	0.3	n.s.
	ΔF	*0.1*	*3*	*0.5*	*0.1*	*0.1*	*0.3*	–	*0.2*	–
Torus-shaped Ni–Si clusters	at.%	0.11	0.23	7.6	10.7	25.6	0.3	0.1	0.23	0.10
	2σ	*0.06*	*0.09*	*0.5*	*0.6*	*0.8*	*0.1*	*0.1*	*0.09*	*0.06*
	F	0.4	5.8	6.9	0.6	3.0	0.4	n.s.	0.2	0.5
	ΔF	*0.2*	*2.1*	*0.5*	*0.1*	*0.1*	*0.2*	–	*0.1*	*0.3*
Grain boundaries	at.%	0.07	0.27	6.32	9.4	26.6	0.53	n.s.	0.18	0.14
	2σ	*0.01*	*0.02*	*0.09*	*0.2*	*0.2*	*0.03*	–	*0.02*	*0.02*
	F	0.25	6.6	5.7	0.5	3.1	0.7	n.s.	0.1	n.s.
	ΔF	*0.05*	*0.5*	*0.1*	*0.1*	*0.1*	*0.1*	–	*0.1*	–

n.s., No significant.

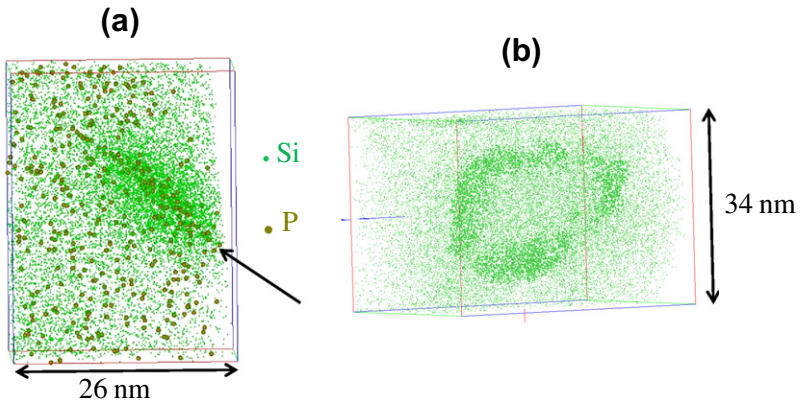

Fig. 4. (a) Ni–Si lenticular rounded cluster, only Si and P atoms are represented. P atoms are located at the center of the cluster. (b) Ni–Si cluster in the form of loop (torus-shaped cluster), only Si atoms are represented. Si atoms, in regions where the Si concentration is higher than 3% at., are emphasized.

at the center of the disc of the Ni–Si clusters. The P concentration reaches 1.5% (from 0.04 at.%). Notably Mo is also enriched to about 4 at.% (from 1.5 at.%). The size of the Mo–P enrichment zone is ≈2 nm. The radii of the Ni–Si torus-shaped clusters are not uniform. The outer torus radius (the distance from the center of the torus to the outer surface of the tube) ranges from 7 to 13 nm, while the inner torus radius (the distance from the center of the torus to the inner surface of the tube) ranges from 5.5 to 10 nm. The average tube radius is 3–4 nm. The number density of Ni–Si torus-shaped clusters is $6 \pm 4 \times 10^{21}$ m^{-3}.

Examples of concentration profiles through a Ni–Si rounded cluster and a Ni–Si torus-shaped cluster are shown in Figs. 5 and 6. The width of the segregation zone is about 9 nm in the case of the rounded cluster and is between 6 and 8 nm for the torus-shaped one. The Ni enrichment and Cr depletion in both types of clusters appears to be similar, but rounded clusters appear to be somewhat more enriched in Si compared to those with a torus-shape.

3.3. Grain boundaries

Two grain boundary slabs were intercepted in analyzed volumes, due to specimen preparation, it is probably the same grain boundary in the two different volumes. An example of a concentration profile plotted through one of them is shown in Fig. 7. The peak Ni and Si concentrations reach 32 at.% (from 8.5 at.%) and 8 at.% (from 1.1 at.%), respectively. The Cr concentration decreases to 8 at.% (from 18.2 at.%) at the center of the segregation zone. The total thickness of the segregated grain boundary slab is between 7 and 10 nm.

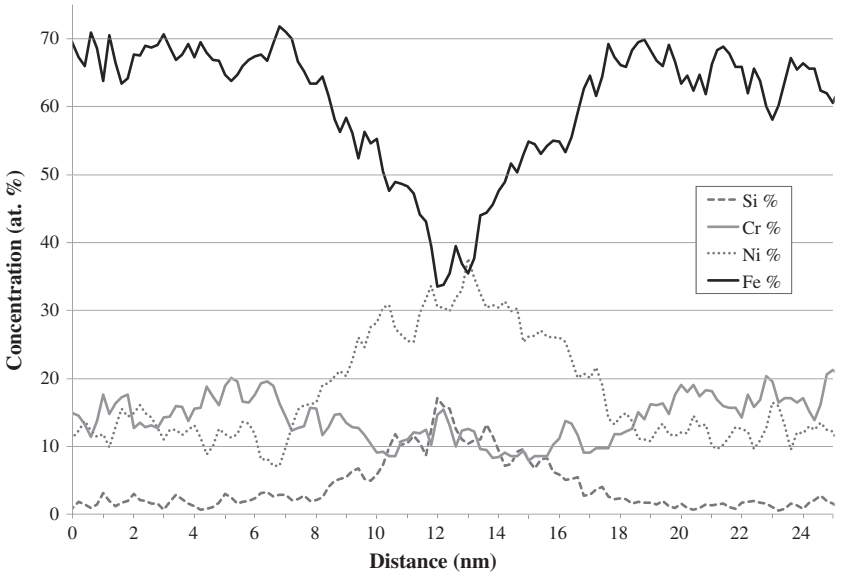

Fig. 5. Concentration profile through a Ni–Si rounded cluster. Fe, Ni, Si and Cr concentrations are plotted as a function of the distance through the cluster. The concentration profile is plotted through a 10 × 10 nm section bin with 0.2 nm step (about 500 atoms per bin).

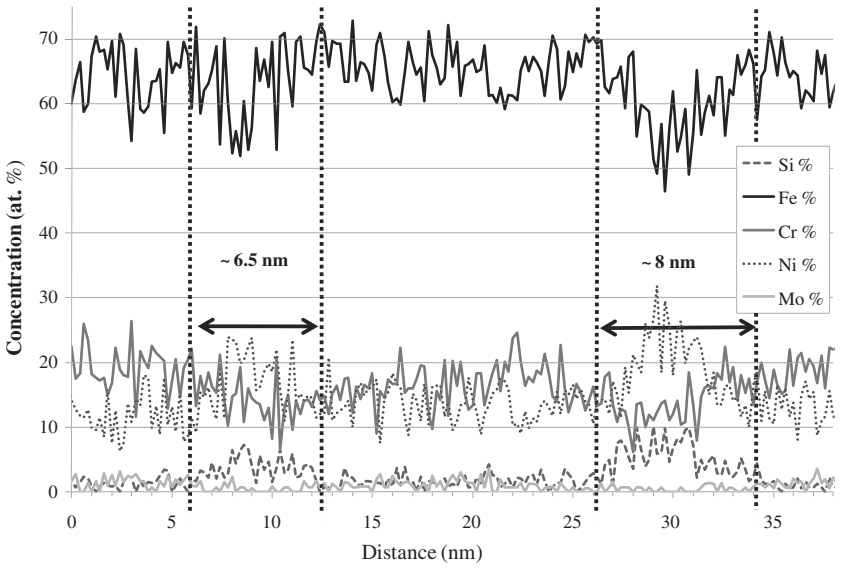

Fig. 6. Concentration profile through a Ni–Si torus-shaped cluster. Fe, Ni, Si, Cr and Mo concentrations are plotted as a function of the distance through the cluster. The concentration profile is plotted through a 5 × 4.5 nm section bin with 0.2 nm step (about 200 atoms per bin).

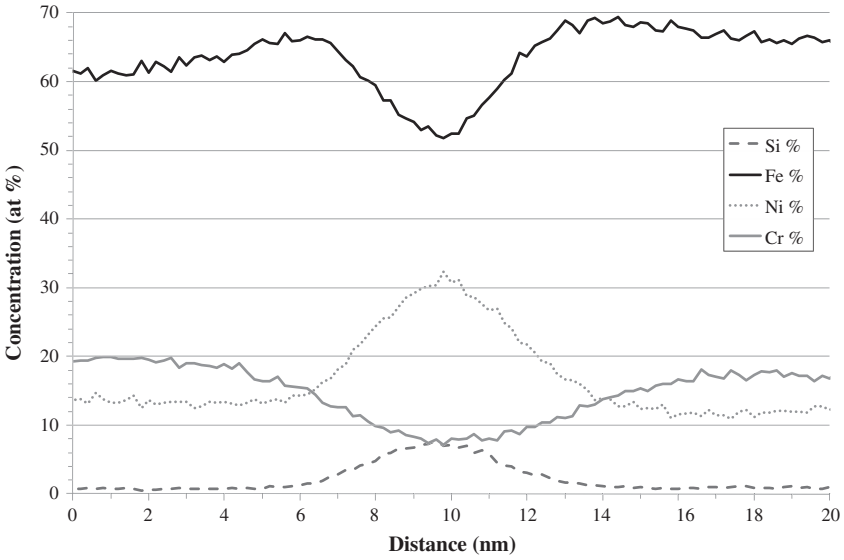

Fig. 7. Concentration profile through a grain boundary. Only Fe, Cr, Ni and Si concentrations are plotted for clarity of the image. The concentration profile is plotted through a 34 × 35 nm section bin with 0.2 nm step (about 7000 atoms per bin).

4. Discussion

All features observed in ion irradiated volumes are enriched in Ni and Si and depleted in Cr. Since the 316SS is sub-saturated with respect to forming intermetallic Ni–Si phases, the only plausible explanation of the presence of these features is radiation-induced segregation (RIS) at defect sinks, which is a well established mechanism that is responsible for the modification of grain boundary composition in irradiated austenitic stainless steels [2]. The different shapes of the features observed here are simply due to the nature of the sinks where segregation occurs: grain boundaries (slabs), dislocation lines (cylindrical features) or Frank loops (rounded and torus-shaped clusters). Although TEM characterization of dislocation loops (Frank loops) was not performed as part of this work, previous results for ion irradiated 316 SS [21,22] showed loop number densities that range from several 10^{20} m^{-3} up to several 10^{22} m^{-3}, the same order of magnitude as the number density of solute clusters found here. Similar observations have been reported for neutron irradiated 316 SS [15]. Further, the torus-shaped clusters observed here are consistent with segregation at large dislocation loops predicted or observed by A. Barbu, as illustrated in Fig. 8 [23]. Segregation at smaller dislocation loops results in the formation of rounded clusters.

The enrichment factors of Ni enrichment and Cr depletion are similar for all the sinks. A comparison of all enrichment factors is reported on Fig. 9. However, Si enrichment at dislocations and loops is systematically more pronounced than observed at the grain boundaries. It is well known that, due to long-range elastic interactions, dislocations are a stronger (biased) sink for self interstitial atoms than for vacancies. The higher enrichment factors at dislocations compared to grain boundaries suggest that Si atoms preferentially diffuse via interstitial mechanism, as previously suggested in [16], whereas Ni and Cr segregate by the inverse Kirkendall vacancy mechanism [2,24].

Solute clusters observed in this work can be compared to those reported in [15] after neutron irradiation of the same material to 12 dpa at 360 °C. The main difference between the two experiments is that irradiation dose rate is $\sim 2 \times 10^{-8}$ dpa s^{-1} in the neutron irradiation case, which is 2×10^4 times less than in ion irradiation case. The irradiation temperature is quasi-similar in both cases. It is well known that the magnitude of RIS depends

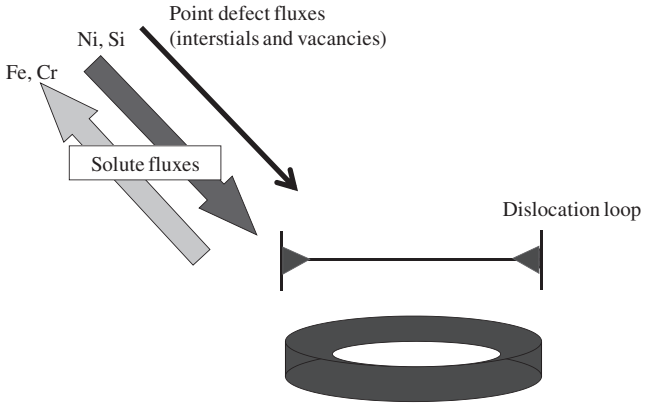

Fig. 8. Schematic representation showing segregation on big dislocation loops.

on the dose rate [2] for a given irradiation temperature. For medium temperatures (between 250 and 400 °C), higher dose rates generally leads to a lower magnitude of RIS [25,26]. In the previous neutron irradiation studies, the Si, Ni and Cr enrichment factors were 56, 5.4 and 0.06 respectively, compared to ≈10, 3.2 and 0.6 for the current ion irradiation case.

Although few results of RIS at grain boundaries under irradiation are reported for doses higher than 5 dpa, a comparison of the RIS at GB in the current work with neutron and proton irradiation results in the literature is shown in Figs. 10 and 11 [4,11,27–32]. It seems that the higher dpa rate ion irradiations in this study produce a slightly higher magnitude of RIS than neutron and proton irradiations at lower dose rates. The lack of results reported in the literature for irradiations at 10 dpa might in part explain this difference. However this result can also be explained in two ways:

First, this result might be due to differences in the experimental characterization techniques. In this work, RIS levels have been obtained using a near atomic scale technique, the atom probe tomography. The theoretical resolution of atom probe tomography approaches the atomic scale and is on the order of 0.5 nm or better. The actual resolution varies from case to case, but is generally better than STEM-EDX techniques. Further, atom probe tomography specifically avoids overlap between the GB and matrix. The

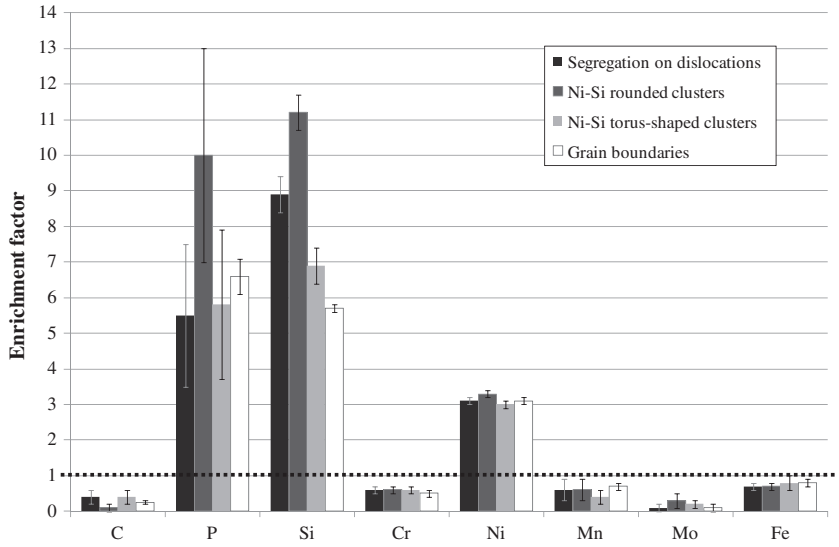

Fig. 9. Comparison between enrichment factors on segregation on dislocations, Ni–Si rounded clusters, Ni–Si torus-shaped clusters and grain boundaries. Enrichment factors are the ratio of the concentration in the object over the concentration in the matrix.

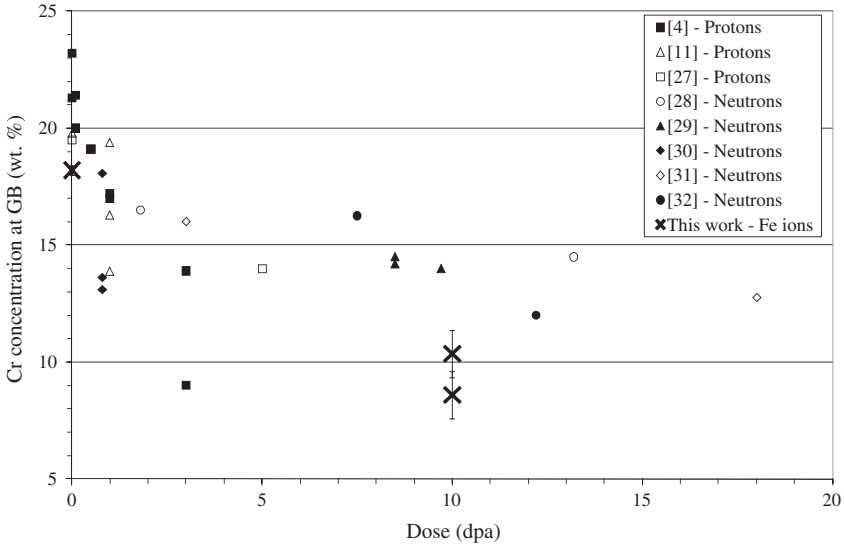

Fig. 10. Grain boundary chromium concentration as a function of dose. Results for the Fe^{5+} ion irradiated 316 SS are compared with those from proton and neutron irradiated 316 SS reported in the literature [4,11,27–32].

resulting smoothing and matrix-GB overlap in the case of STEM-EDX would lead to underestimation of peak magnitude of RIS.

Secondly, several studies have shown that radiation-induced levels can depend on grain boundary misorientation angles [33–36] and can also vary along the same grain boundary [37]. Duh et al. [33] reported Cr segregation differences up to 4 at.% and Edwards et al. [36] found Ni segregation difference of 5 at.% from one grain boundary to another, in an austenitic steel proton irradiated at 1 dpa and neutron irradiated at 6 dpa, respectively. An absolute variation of 3 at.% of the Cr concentration was reported by Simonen et al. [37] along the same grain boundary in an austenitic steel irradiated at 10 dpa with ions. As shown in Figs. 10 and 11, some variations of the composition along the grain boundary can be observed in this study. Thus variations of local segregation levels may explain some differences between results found in this study and results from the literature.

5. Conclusions

In this work, a 316 austenitic stainless steel, irradiated with Fe^{5+} ions to 10 dpa, has been investigated by atom probe tomography.

Different intragranular features were observed, including cylindrical features, rounded clusters and torus-shaped clusters that are certainly formed by RIS to sinks consisting of network dislocations, small and bigger dislocation loops respectively.

For the first time, grain boundary segregation has been observed at the near atomic scale in an irradiated austenitic stainless steel. These measurements were enabled by the use of a focused ion beam instrument for specimen preparation for APT. The magnitude of RIS measured here is higher than results found in the literature. This suggests that other techniques may underestimate the peak values of RIS. However, variations in RIS in a particular boundary and between different boundaries may also play a role.

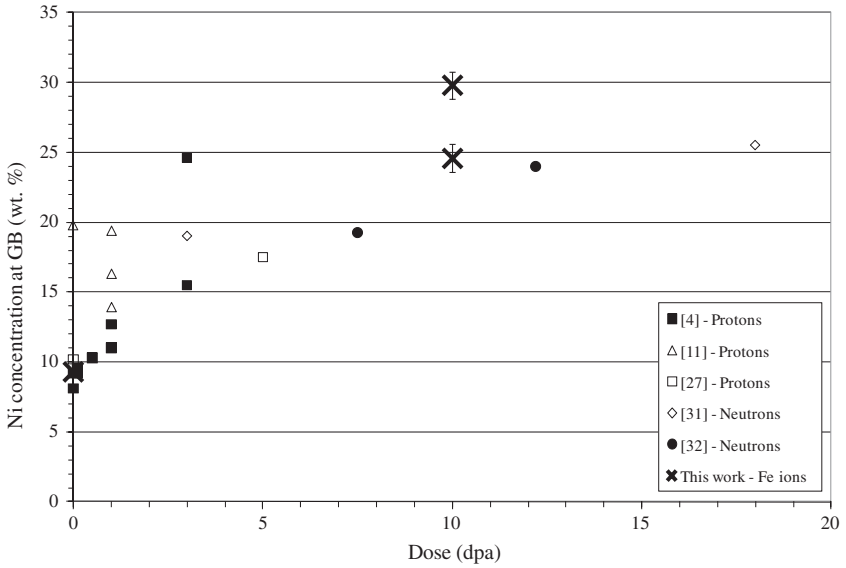

Fig. 11. Grain boundary nickel concentration as a function of dose. Results for the Fe^{5+} ion irradiated 316 SS are compared with those from proton and neutron irradiated 316 SS reported in the literature [4,11,27,30,31].

Acknowledgements

This work is a part of the research program of the EDF-CNRS joint laboratory EM^2VM (Study and Modeling of the Microstructure for Ageing of Materials) and was also partly supported by a 2009 French national grant "For Women in Science" from L'Oréal – Unesco – Académie des Sciences. The specimen preparation and atom probe tomography measurements were carried out in the UCSB Materials Research Laboratory Microstructure and Microanalysis Facility supported by the MRSEC Program of the National Science Foundation under award No. DMR05-20415. The authors are grateful to Yves Serruys from CEA/SRMP for performing ion irradiation on the JANNuS plateform at CEA Saclay (France). The authors would like to thank Charly Vaudolon for the sample and specimen holder preparation.

References

[1] G.S. Was, P. Andresen, JOM 44 (1992) 8.
[2] S.M. Bruemmer, E.P. Simonen, P.M. Scott, P.L. Andresen, G.S. Was, J.L. Nelson, J. Nucl. Mater. 274 (1999) 299–314.
[3] T.R. Allen, G.S. Was, E.A. Kenik, J. Nucl. Mater. 244 (1997) 278–294.
[4] T.R. Allen, J.T. Busby, G.S. Was, E.A. Kenik, J. Nucl. Mater. 255 (1998) 44–58.
[5] T.R. Allen, J.I. Cole, E.A. Kenik, G.S. Was, J. Nucl. Mater. 376 (2008) 169–173.
[6] P.L. Andresen, P.H. Chou, M.M. Morra, J.L. Nelson, R.B. Rebak, Metall. Mater. Trans. A 40A (2009) 2824–2836.
[7] J.T. Busby, G.S. Was, E.A. Kenik, J. Nucl. Mater. 302 (2002) 20–40.
[8] H.M. Chung, W.E. Ruther, J.E. Sanecki, A. Hins, N.J. Zaluzec, T.F. Kassner, J. Nucl. Mater. 239 (1996) 61–79.
[9] D.L. Damcott, T.R. Allen, G.S. Was, J. Nucl. Mater. 225 (1995) 97–107.
[10] E.A. Kenik, J. Nucl. Mater. 187 (1992) 239–246.
[11] G.S. Was, T.R. Allen, J.T. Busby, J. Gan, D. Damcott, D. Carter, M. Atzmon, E.A. Kenik, J. Nucl. Mater. 270 (1999) 96–114.
[12] R.D. Carter, D.L. Damcott, M. Atzmon, G.S. Was, S.M. Bruemmer, E.A. Kenik, J. Nucl. Mater. 211 (1994) 70–84.
[13] V.J. Keast, D.B. Williams, J. Microsc. 199 (2000) 45–55.
[14] K. Nakata, I. Masaoka, J. Nucl. Mater. 150 (1987) 186–193.
[15] A. Etienne, P. Pareige, B. Radiguet, J.-P. Massoud, C. Pokor, J. Nucl. Mater. 382 (2008) 64–69.
[16] A. Etienne, B. Radiguet, P. Pareige, J. Nucl. Mater. 406 (2010) 251–256.
[17] P. Trocellier, Y. Serruys, S. Miro, E. Bordas, S. Pellegrino, S. Vaubaillon, M.O. Ruault, S. Henry, O. Kaïtasov, Nucl. Inst. Methods Phys. Res. Sec. B 266 (2008) 3178–3181.
[18] Y. Serruys, M.-O. Ruault, P. Trocellier, S. Henry, O. Kaïtasov, P. Trouslard, Nucl. Inst. Methods Phys. Res. Sec. B 240 (2005) 124–127.
[19] J.F. Ziegler, J.P. Biersack, U. Littmark, The Stopping and Range of Ions in Solids, Pergamon Press, New York, 1985.
[20] M.K. Miller, K.F. Russell, Ultramicroscopy 107 (2007) 761–766.
[21] C. Pokor, J.-P. Massoud, P. Pareige, J. Garnier, D. Loisnard, P. Dubuisson, B. Doisneau, Y. Bréchet, in: 12th International Conference on Environmental Degradation of Materials in Nuclear Systems – Water Reactors, The Minerals, Metals and Materials Society, Salt Lake City, 2005.
[22] J. Gan, E.P. Simonen, S.M. Bruemmer, L. Fournier, B.H. Sencer, G.S. Was, J. Nucl. Mater. 325 (2004) 94–106.
[23] A. Barbu, Contribution à l'étude des changements de phase sous irradiation, Rapport CEA-R-4936, CEA-SRMP Saclay, 1979.
[24] S.J. Zinkle, P.J. Maziasz, R.E. Stoller, J. Nucl. Mater. 206 (1993) 266–286.
[25] T.R. Allen, J.I. Cole, C.L. Trybus, D.L. Porter, H. Tsai, F. Garner, E.A. Kenik, T. Yoshitake, Joji Ohta, J. Nucl. Mater. 348 (2006) 148–164.
[26] G.S. Was, S.M. Bruemmer, J. Nucl. Mater. 216 (1994) 326–347.
[27] G. Was, J. Busby, T. Allen, E. Kenik, A. Jenssen, S. Bruemmer, J. Gan, A. Edwards, P. Scott, P. Andresen, J. Nucl. Mater. 300 (2002) 198–216.
[28] J. Walmsley, B.P. Spellward, S. Fisher, A. Jenssen, in: R.E. Gold, E.P. Simonen (Eds.), Proceedings of the 7th International Symposium on Environmental Degradation of Materials in Nuclear Power Systems Water Reactors, NACE International, Houston, TX, 1995, p. 985.
[29] K. Asano, K. Fukuya, K. Nakata, M. Kodoma, in: D. Cubicciotti, (Ed.), Proceedings of the 5th International Symposium on Environmental Degradation of Materials in Nuclear Power Systems Water Reactors, Monterey, CA, American Nuclear Society, La Grange Park, IL, 1992, p. 838.
[30] K. Fukuya, M. Nakano, K. Fujii, T. Torimaru, J. Nucl. Sci. Technol. 41 (2004) 594.
[31] J.F. Williams, T.R. Mager, P. Spellward, J. Walmsley, M. Koyama, I. Suzuki, H. Mimaki, in: 8th International Symposium on Environmental Degradation of Materials in Nuclear Power Systems – Water Reactors, Amelia Island, FL, USA, August 10–14, 1997, p. 725.
[32] D.J. Edwards, E.P. Simonen, F.A. Garner, L.R. Greenwood, B.M. Oliver, S.M. Bruemmer, J. Nucl. Mater. 317 (2003) 32.
[33] T.S. Duh, J.J. Kai, F.R. Chen, J. Nucl. Mater. 283–287 (2000) 198–204.
[34] T.S. Duh, J.J. Kai, F.R. Chen, L.H. Wang, J. Nucl. Mater. 294 (2001) 267.
[35] S. Watanabe, Y. Takamatsu, N. Sakaguchi, H. Takahashi, J. Nucl. Mater. 283–287 (2000) 152–156.
[36] D. Edwards, F. Garner, E. Simonen, S. Bruemmer, EPRI, Palo Alto, CA, 2001, p. 1001497.
[37] E.P. Simonen, L.A. Charlot, S.M. Bruemmer, J. Nucl. Mater. 225 (1995) 117–122.